

Article

# Design of a Remote, Multi-Range Conductivity Sensor

Georgiana Dima \*, Anna Radkovskaya, Christopher J. Stevens, Laszlo Solymar and Ekaterina Shamonina

Department of Engineering Science, University of Oxford, Oxford OX1 3PJ, UK

\* Correspondence: georgiana.dima@eng.ox.ac.uk

**Abstract:** So far, research on remote conductivity detection has primarily focused on large conductivities. This paper examines the entire conductivity range, proposing a method that can be adapted to the desired application. The optimization procedure for the different regions is presented and discussed. Specific interest is given to the low-conductivity range, below 10 S/m, which covers human body tissues. This could lead to applications in body imaging, especially for induction tomography. Conductivities below 12.5 S/m are extracted experimentally with an error below 10%.

**Keywords:** conductivity detection; remote sensing; low conductivity

## 1. Introduction

Eddy current analysis is an established non-contact sensing technique [1,2]. A wide range of antenna and metamaterial arrays [3–6] has been developed; these arrays are involved in eddy current sensing techniques. Most publications in the field focus on non-destructive testing (NDT) applications, which include thickness measurements [7–17], detection of cracks and defects [18–28], as well as measurements of conductivity  $\sigma$  [10–14,29–32] and permeability  $\mu$  [33–35] in highly conductive samples. These applications cover only a fraction of the conductivity spectrum, although detecting mid-range and low  $\sigma$  can lead to exciting applications.

For the mid-range conductivity spectrum, a recent area that has elicited interest is in creating conductive 3D-printed materials [36–46]. Once a 3D sample has been printed, it is hard to assess if the material has the desired properties without potentially damaging the sample. For example, the conductivity of Electrifi, one of the most widely used 3D-printed filaments, can be heavily influenced by printing conditions, but this can only be assessed through invasive methods. The conductivity of these 3D-printed materials ranges between 10 and 50,000 S/m, which in this paper will be broadly classified as the mid-range  $\sigma$  space. The conductivities of various 3D-printed filaments used in the literature are described in [41].

Another area with significant potential is that of biomedical imaging. Inductive tomography [47,48] is a new, promising imaging method where transmitting and receiving coils are used to map the conductivities and permittivities of different body tissues and, ultimately, image through them or monitor any abnormalities. One such application is detecting the presence of water in the lungs. At 50 MHz, as shown in Table 1, the conductivity range for the lung is between 0.28 S/m (when the lung is inflated) and 0.52 S/m (when the lung is deflated). If water is present in the lungs, this conductivity rises to around 0.5 S/m (for the inflated lung) and 0.7 S/m (for the deflated lung) [49–51]. Such differences can be detected by the sensor and lead to further tests being performed on the patient. The applicability of eddy current testing in a similar area is shown in [52,53], where the breathing cycle and low oxygen concentrations are monitored. Currently, more in-depth research is required to optimize and transform this idea into functional equipment. Although several publications have investigated high-conductivity detection, few have investigated methods of detecting low conductivity. Yin et al. [31] investigated the conductivity and the thickness of a salty water solution and managed to detect these properties with an accuracy of 3%.



**Citation:** Dima, G.; Radkovskaya, A.; Stevens, C.J.; Solymar, L.; Shamonina, E. Design of a Remote, Multi-Range Conductivity Sensor. *Sensors* **2023**, *23*, 9711. <https://doi.org/10.3390/s23249711>

Academic Editors: Wilmar Hernandez, Guillermo Villanueva, Sabina Merlo, Faisal Mohd-Yasin, Aldo Minardo, Nunzio Cennamo, Cosimo Trono and Andreas Savakis

Received: 6 November 2023

Revised: 30 November 2023

Accepted: 4 December 2023

Published: 8 December 2023



**Copyright:** © 2023 by the authors. Licensee MDPI, Basel, Switzerland. This article is an open access article distributed under the terms and conditions of the Creative Commons Attribution (CC BY) license (<https://creativecommons.org/licenses/by/4.0/>).

However, the range of conductivities considered was relatively narrow, with only four considered values (3.7, 6.4, 8.3, 10.2 S/m). Additionally, a scaling factor was applied in [31] to ensure that the analytical model used matched the experimental values. Permittivity was not considered; however, for low  $\sigma$  in the biomedical application discussed here, this parameter is essential.

The present paper focuses on identifying a design procedure for probes that will detect  $\sigma$  in each of the three aforementioned cases (low, mid, and high range  $\sigma$ ) and will present results that support the design. Specific focus will be given to detecting conductivities similar to those in the human body, as novel applications can emerge from being able to differentiate tissues depending on their conductivity. The conductivity and permittivity of some biological tissues at the operation frequency of 50 MHz are presented in the table below (Table 1) as obtained from [49–51].

**Table 1.** Conductivity,  $\sigma$ , and relative permittivity,  $\epsilon_r$ , for various body tissues at 50 MHz [49–51].

Tissue	$\sigma$ [S/m]	$\epsilon_r$
Blood	1.19	94.2
Muscle	0.68	77.1
Heart	0.65	118.0
Deflated Lung	0.52	81.3
Inflated Lung	0.28	41.3
Dry Skin	0.41	107.2
Fat	0.03	6.9

First, the analytical model and the working principle of the probe will be presented in Section 2.1. The setup used for the numerical simulations in CST Microwave Studio will be introduced in Section 2.2, while the experimental setup and the data post-processing will be described in Section 2.3. In Sections 3.1 and 3.2, the analytical results for various system parameters will be provided in order to justify the design criteria suggested. The focus will then shift toward the low conductivity range in Section 3.3, where the conductivities of water and salt will be extracted from experiments. The conclusion of the paper will be outlined in Section 4, where final recommendations for the design procedures will be offered.

## 2. Materials and Methods

### 2.1. Analytical Model

The sensing probe used relies on a single resonating element with one loop of radius  $r_0$  and wire thickness  $w$ , tuned to a resonating frequency  $f_0$  using a lumped capacitor. The probe is placed a distance  $h$  above a testing material of thickness  $t$ , conductivity,  $\sigma$ , relative permittivity  $\epsilon_r$ , and relative permeability  $\mu_r$ . The testing sample dimensions in the horizontal plane are expected to be much larger than the probe diameter. This configuration is shown schematically in Figure 1.

When the resonator is excited, a magnetic flux proportional to the current flowing through the circuit is generated. The constant of proportionality between the magnetic flux and the current is called the self-inductance ( $L$ ) of the element. If the coil is placed near a material with different electromagnetic properties than air, a time-varying magnetic flux will generate eddy currents within the material. This changes both the magnitude and the direction of the overall magnetic flux, resulting in a complex self-inductance. In other words, the presence of a testing material beneath an excited coil changes the coil's self-inductance. Figure 2 shows the absolute value and orientation of the magnetic field in the plane  $y = 0$ , as obtained from analytical simulations for different values of  $\sigma$  (0.1, 10, 1000 S/m). Looking at the field strength at  $z = -50$  mm, it is evident that as the conductivity increases from 0.1 S/m to 10 S/m and 1000 S/m, the magnitude of the field

strength drops from 1.33 A/m to 0.5 A/m and then to  $8.9 \times 10^{-10}$  A/m. This supports the fact that, as conductivity increases, the depth of penetration decreases, and so does the magnitude of the field. The overall orientation of the magnetic field is also altered by the presence of a conductive sample. This is the result of the mirroring field from the surface of the sample, which cancels out some of the field within the coil. This will be further explained in Section 3.1, where the similarities between a mirror and an ideal conductor will be presented.

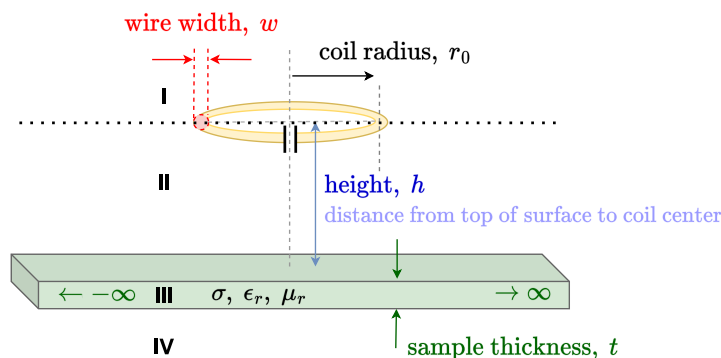


**Figure 1.** Schematic diagram of the system showing all the relevant geometrical parameters. Regions I–IV represent the regions where the material properties change. Between these regions, boundary conditions are imposed as described in Section 2.1.

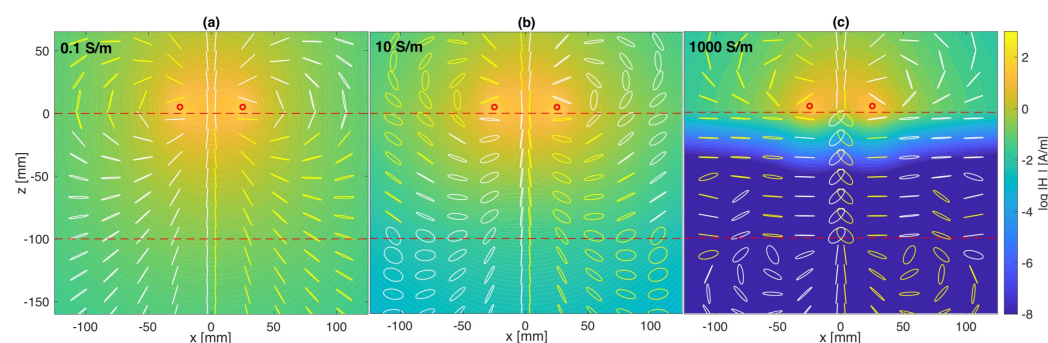


**Figure 2.** Logarithmic value of magnitude and polarization of the magnetic field,  $H$ , for a system with a coil of radius,  $r_0 = 25$  mm, coil width,  $w = 1$  mm, resonant frequency,  $f_0 = 50$  MHz, free-space quality factor,  $Q_0 = 250$ , height,  $h = 5$  mm, sample thickness,  $t = 10$  cm, and relative permittivity and permeability,  $\mu_r = \epsilon_r = 1$ . The conductivity of the sample is: (a) 0.1 S/m; (b) 10 S/m; (c) 1000 S/m.

This change can be found by generalizing the partial differential equation used by Dodd and Deeds [54] for vector potential  $\mathbf{A}$  due to an applied current density  $\mathbf{i}_0$ :

$$\nabla^2 \mathbf{A} = -\mu \mathbf{i}_0 + \mu \sigma \frac{\partial \mathbf{A}}{\partial t} + \mu \epsilon \frac{\partial^2 \mathbf{A}}{\partial t^2} + \epsilon \partial \left( \frac{1}{\mu} \right) \times (\nabla \times \mathbf{A}) \tag{1}$$

Equation (1) is derived from Maxwell’s equations [55], ensuring full applicability. The geometry in Figure 1 is divided into four layers (I–IV), which are isotropic, linear, and homogeneous. The excitation is considered filamentary and is situated between layers I and II. Simplifications similar to those in [54] are performed on Equation (1). The main difference is that, here, as in [56,57], the term  $\mu \epsilon \delta^2 \mathbf{A} / \delta t^2$  is considered relevant and accounted for in the analytical model. For high conductivity and small frequencies, this term is usually ignored in the literature. Using this term will allow for an accurate estimation of low conductivities. Once the simplifications are made, the equation is solved and the boundary conditions between every two layers are used to determine the vector potential in each region. Here, the self-inductance of a coil is approximated to be equivalent to the mutual inductance between two filaments, spaced a geometric mean distance ( $R_{\text{GMD}}$ ) apart, similar

to Maxwell's approach for calculating self-inductance at higher frequencies [58].  $R_{\text{GMD}}$  can be found in [59–61]. The full derivation of the vector potential and the calculation of self-inductance is provided in Appendix A. The final expression for the inductance is as follows:

$$L = L_r + jL_i = \pi r_0^2 \mu_0 \int_0^\infty \alpha_0 J_1^2(\alpha r_0) \left( e^{\alpha_0 R_{\text{GMD}}} + \frac{(\alpha_0^2 - \alpha_1^2) e^{-\alpha_0 2h} (e^{2\alpha_1 t} - 1)}{(\alpha_1 + \alpha_0)^2 e^{2\alpha_1 t} - (\alpha_0 - \alpha_1)^2} \right) d\alpha \quad (2)$$

Two important parameters of the coils will be simulated, following the inductance calculation: the resonant frequency (denoted as  $f_0$  in free space and  $f_{\text{res}}$  in the vicinity of a material) and the quality factor ( $Q_0$  in free space and  $Q$  in the vicinity of a material). In free space, these parameters are given by

$$f_0 = \frac{1}{2\pi\sqrt{LC}} \quad (3)$$

$$Q_0 = \frac{2\pi f_0 L}{R} \quad (4)$$

When a material is present, the derivation becomes somewhat more complicated, but a reasonable approximation is found to be

$$f_{\text{res}} = \frac{1}{2\pi\sqrt{L_r C}} \quad (5)$$

$$Q = \frac{2\pi f_{\text{res}} L_r}{R - j2\pi f_{\text{res}} L_i} \quad (6)$$

The circuit analysis shows that the real part of the new inductance,  $L_r$ , becomes the new inductance of the coil, while the imaginary part,  $L_i$ , contributes to the resistance in proportion to the resonant frequency.

## 2.2. Numerical Model

CST Microwave Studio 2020 was used as a numerical tool to offer more points of comparison for the analytical and experimental results. Figure 3 shows the CST model used for the simulations that were performed here. The mesh distribution is displayed in the figure. The bounding box that is filled with air is 500 mm away from the structure in all directions and the boundary conditions are open (add space). The background mesh is set at 5 cells per wavelength. The local mesh for the coil is set at 0.5 mm, and for the sample, it is 15 mm. The coil is tuned using a lumped capacitor, placed in series with the S-parameter excitation source, which has an impedance of 50 Ohms. The sample is designed to be six times wider than the coil diameter, as this size has been determined to be large enough for the sample to be approximated as infinite, thus comparable with the analytical model, yet small enough to allow for computation within a reasonable timeframe. The accuracy of the S-parameter measurements is set at 1.5%. The  $Z_{11}$  parameter is extracted and then the resonant frequency is extracted as the frequency at which  $Z_{11}$  reaches a minimum, while the quality factor is obtained by calculating the ratio between the bandwidth of the  $Z_{11}$  curve and the resonant frequency.

## 2.3. Experimental Setup

Figure 4a shows the schematic of the experimental arrangement and Figure 4b–e display some photographs of the experiment. The coils used were created by winding a single loop of wire into a coil-shaped mold that was 3D-printed with high-impact polystyrene (HIPS). This material was chosen for its low dielectric constant, ensuring that the structural support would not affect the overall results. To secure the coil in place, a sheet of Rohacell foam was utilized. Given its properties, very similar to those of air, this foam is not expected

to significantly impact the results either. The coil, with a radius of  $r_0 = 25$  mm and wire width of  $w = 1.04$  mm was placed at a distance of  $h = 5.32 \pm 0.11$  mm from the sample, which is represented by a water tank measuring  $300 \times 300$  mm, with a water layer thickness of  $t = 100$  mm. The conductivity of the water was gradually changed by adding salt. The conductivity after each salt-adding iteration was measured using a Hanna HI-8633 multi-range conductivity meter.

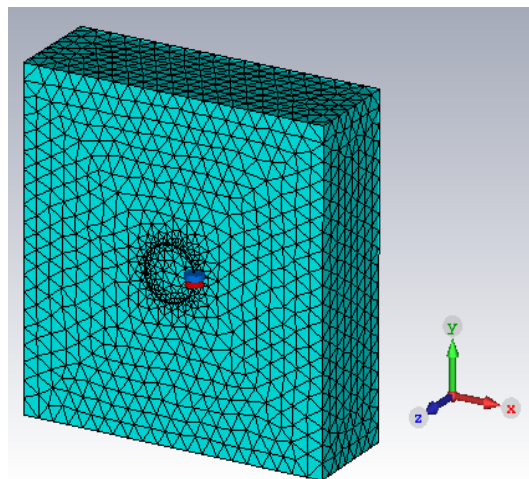


**Figure 3.** CST Microwave Studio model with the shown mesh. The present components are the conductive sample, the coil, the tuning capacitor, and the excitation port, placed in series with the capacitor.

The coil is connected to an 8753ES Hewlett Packard Vector Network Analyzer (VNA) through the SMA connector and a  $50 \Omega$  cable whose impact was removed through a standard calibration procedure. The  $S_{11}$  parameter was obtained for 1601 points in the frequency spectrum. The power used was 0 dBm and the number of averages for each data point was 2. For each  $\sigma$ , 20 data points were obtained. The  $S_{11}$  parameter was used to extract the impedance spectrum,  $Z_{11}$ , through the following formula, where  $Z_L$  is the known impedance and  $50 \Omega$  is the load of the VNA:

$$Z_{11} = Z_L \frac{S_{11} + 1}{S_{11} - 1} \quad (7)$$

The data extracted are then filtered by using a Savitzky–Golay filter with a window length of 32 and order 2, with 10,000 values interpolated in the frequency range considered in order to increase the accuracy of  $Q$  estimation. The resonant frequency  $f_{\text{res}}$  is extracted as the frequency where the impedance parameter reaches a minimum and the quality factor  $Q$  is obtained by dividing this resonant frequency through the 3 dB bandwidth, BW. In this way, the free space properties of the coil were estimated to be  $f_0 = 49.777$  MHz and  $Q_0 = 256$ . Once  $f_{\text{res}}$  and  $Q$  are extracted for different conductivity samples, depending on the value of  $f_{\text{res}}$ , one of them becomes the main extraction parameter. The extraction is performed using the bisection method, where the conductivity of the analytical model is changed until the analytical value of the extraction parameter matches the experimental one. Two extraction parameters are proposed, namely the quality factor and the resonant frequency for which an analytical model is provided in Section 2.1. Sections 2.1 and 3.1 discuss the parameters that should be used for extraction in each range, while Section 3.2 describes the proposed extraction procedure.

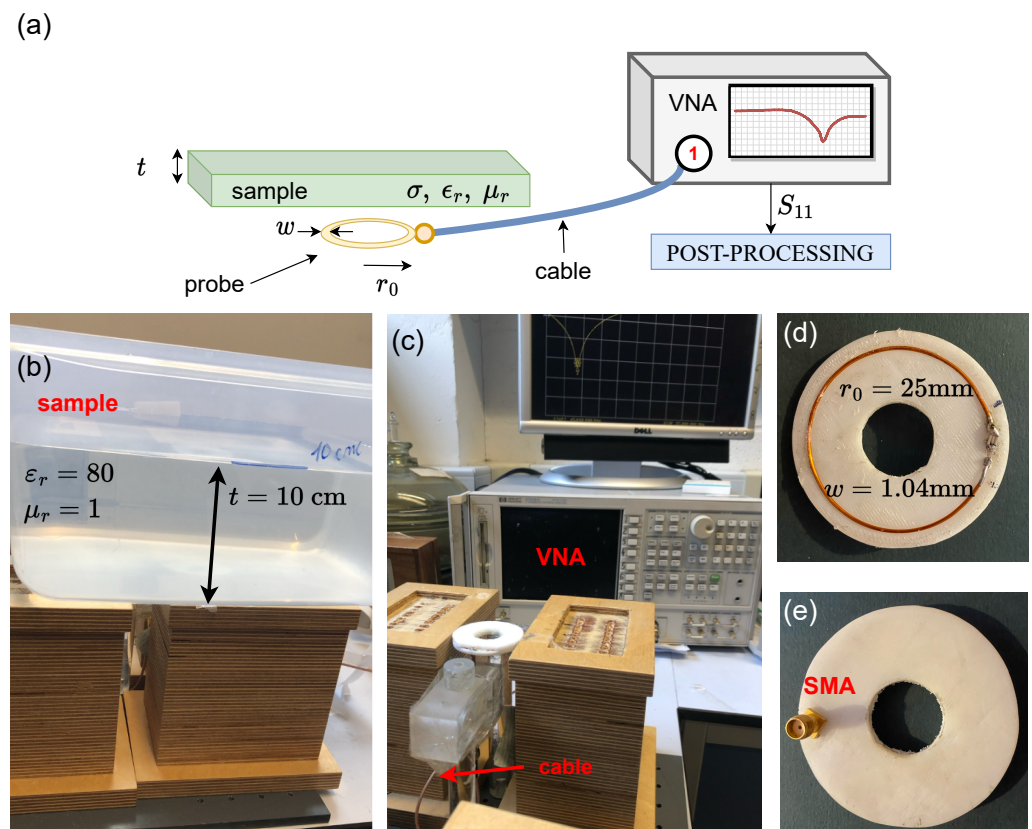


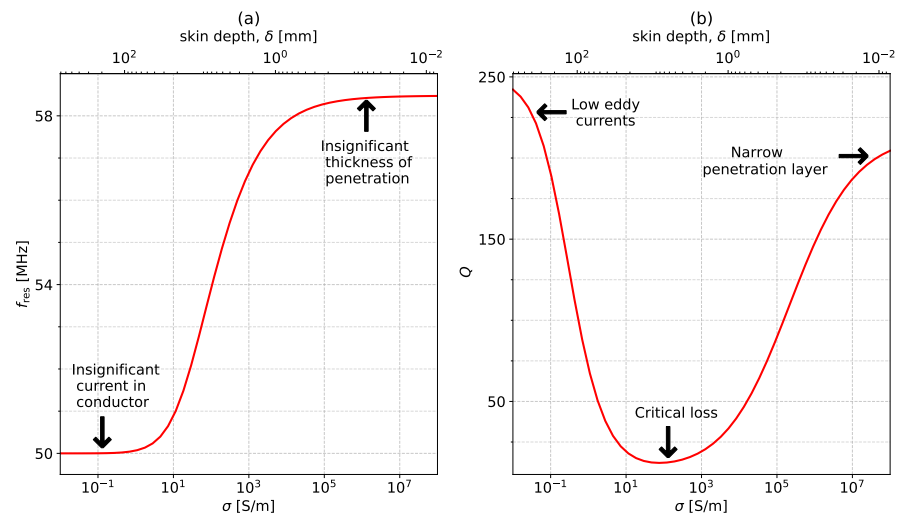
**Figure 4.** Experimental arrangement: (a) schematic representation, (b) sample photograph, (c) photograph of the coil and VNA with no sample, and (d,e) top and bottom photographs of the probe.

### 3. Results

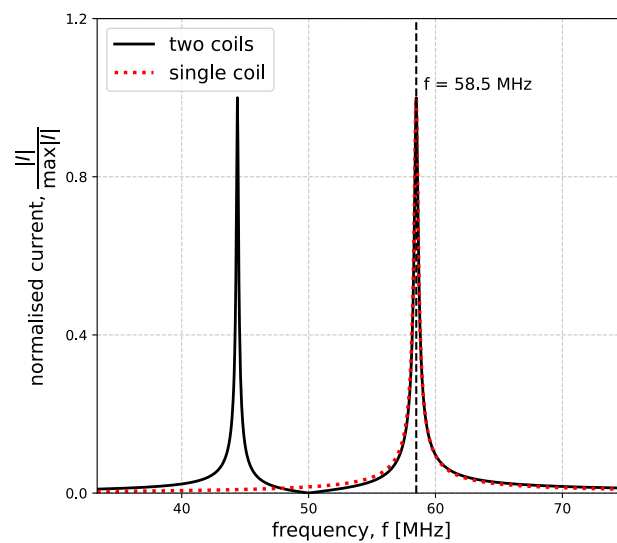
#### 3.1. $Q$ and $f_{\text{res}}$ Analytical

Figure 5 shows the variation of  $f_{\text{res}}$  and  $Q$  with conductivity. The coil has  $r_0 = 25$  mm,  $w = 1$  mm,  $f_0 = 50$  MHz,  $Q_0 = 250$ , and the sample used ( $t = 10$  cm and  $\mu_r = \epsilon_r = 1$ ) changes its conductivity in the range of 0.01 S/m to  $10^8$  S/m. The coil is placed at a distance of  $h = 5$  mm. As  $\sigma$  increases,  $f_{\text{res}}$  starts increasing steadily and then plateaus to a constant value. This constant value is equivalent to the case of an ideal conductor that behaves like a mirror due to the fact that the depth of penetration, known as the skin depth, is very narrow. The reduction in the depth of penetration is clearly presented in Figure 2, where a conductivity of 1000 S/m results in the magnetic field only being significant at the top of the surface. In the case of an ideal conductor, the magnetic field is fully canceled out as a consequence of Lenz's Law, and the system can be interpreted as containing two coils placed axially in free space, a distance of  $2h = 10$  mm apart. However, because the conductor acts as a mirror, only the asymmetrical mode for the coupled resonators is supported. In the case of axially coupled resonators, this mode corresponds to the upper peak in the current spectra. The position of this peak is, therefore, the position where the resonance of a coil above a sample with very large conductivity will settle. This correlation is clearly illustrated in Figure 6. The figure displays the normalized absolute value of the current spectra for a single coil placed above a conductive sample with  $\sigma = 10^8$  S/m (red dotted line) and the normalized absolute value of the current spectra for one of the coils in a system of two coils placed axially in free space a distance  $2h$  apart (black line). The mutual inductance for the coil is calculated in a similar manner as the self-inductance by assuming that the coils are filamentary and the distance between them is no longer  $R_{\text{GMD}}$ , as in Section 2.1, but  $2h$ . The upper peak of the coupled system perfectly matches the resonant peak in the single-coil system placed above a nearly perfect conductor. In the case

of non-ideal conductors, the reflection coefficient is lower than 1, leading to a combination of transmission and reflection and, hence, intermediary resonant frequency values.



**Figure 5.** Variation of (a)  $f_{\text{res}}$  and (b)  $Q$  with conductivity,  $\sigma$ . The system parameters are  $r_0 = 25$  mm,  $w = 1$  mm,  $f_0 = 50$  MHz,  $h = 5$  mm,  $Q_0 = 250$ ,  $t = 10$  cm, and  $\mu_r = \epsilon_r = 1$ .



**Figure 6.** Absolute normalized current for a coil placed  $h = 5$  mm above a 10 cm thick conductor of  $\sigma = 10^8$  S/m (red dotted line) and for a system of two axially coupled coils placed  $2h = 10$  mm apart (black line). The coils have  $r_0 = 25$  mm,  $w = 1$  mm,  $f_0 = 50$  MHz and  $Q_0 = 250$ .

Moving on to the quality factor:  $Q$  starts high for very low conductivities and then drops in the mid-range, where it remains relatively steady. This constant region is followed by an increase in  $Q$  for high-conductivity values. This behavior is a consequence of two competing phenomena. The first one concerns energy dissipation in the sample material due to the generated eddy and displacement currents. These currents increase as the conductivity increases. The second phenomenon is the decline of the skin depth as the conductivity increases. This means that the regions where currents are created become smaller, leading to lower losses. For low  $\sigma$ , the first phenomenon is dominant, and, as conductivity increases, the second mechanism becomes more relevant, ultimately being the dominant of the two. The conductivity where the transition occurs depends on multiple factors, such as the thickness of the sample, the operating frequency, and the geometrical parameters of the split-ring resonator.

From an extraction perspective, these two parameters cover the entire conductivity range.  $Q$  changes sharply in the low and high ranges while  $f_{\text{res}}$  changes significantly in the mid-range of  $\sigma$ . The decision on where to switch between the two can be made depending on  $f_{\text{res}}$ . For a specific known geometry, the two frequencies at which the transition between the two detection methods occurs can be calculated analytically, depending on the specific accuracies that can be achieved in extracting  $f_{\text{res}}$  and  $Q$ .

As mentioned above, these curves are impacted significantly by certain parameters. One of these critical parameters is the thickness of the sample. Figure 7 shows the variation in resonant frequency and quality factor as  $\sigma$  varies in the range of 0.01 S/m to  $10^8$  S/m for four values of sample thicknesses (0.5, 2, 10, 100 mm). The parameters of the system are the same as in Figure 5, except for the thickness that takes the aforementioned values. The dotted lines represent the positions where the skin depth is the same as the thickness of the sample. In free space and for very large conductivities, the curves have the same characteristics. As the thickness becomes smaller, larger conductivities are required in order to notice changes in the resonant frequency. This is because, at low conductivities, the magnitude of the generated eddy currents is lower, and so is the accessible depth of penetration due to the limited sample thickness. This results in lower overall perturbations from the free-space scenario. When the depth of penetration decreases to the skin depth due to the increase in  $\sigma$ , the curves for both resonant frequency and quality factor start converging to the curve for  $t = 100$  mm. From the quality factor perspective, a thinner sample requires higher current densities (hence, higher conductivities) for the transition between the two phenomena mentioned above to occur because the depth of penetration is limited to the thickness of the sample. Overall, thinner specimens results in less resonant frequency and quality factor changes for conductivities with skin depth larger than  $t$ .

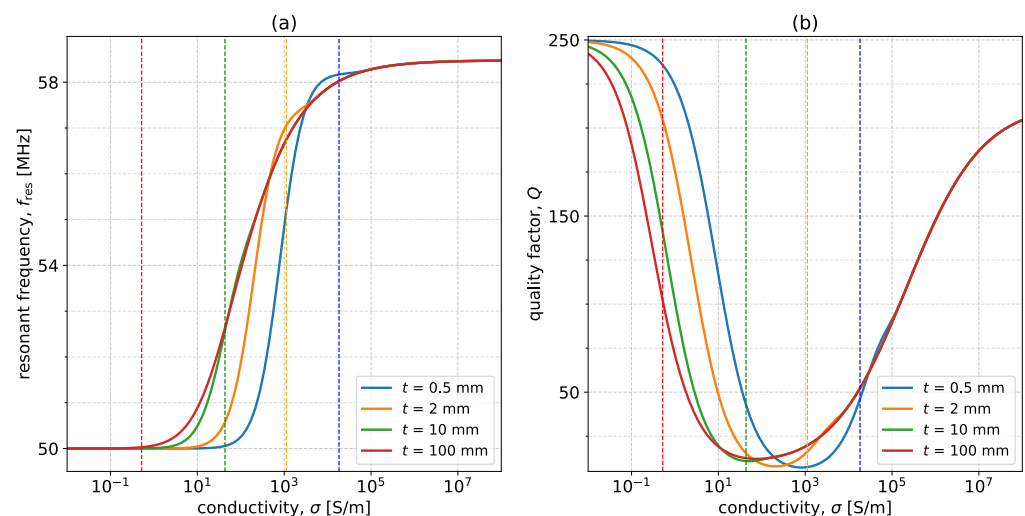


**Figure 7.** Variation of (a)  $f_{\text{res}}$  and (b)  $Q$  with conductivity,  $\sigma$ , for four values of thickness: 0.5 mm (blue), 2 mm (orange), 10 mm (green), and 100 mm (red). The parameters of the system are  $r_0 = 25$  mm,  $w = 1$  mm,  $f_0 = 50$  MHz,  $h = 5$  mm,  $Q_0 = 250$ , and  $\mu_r = \epsilon_r = 1$ . The dotted lines indicate positions where the skin depth is equal to the sample thickness.

Another important parameter is the ratio between the height,  $h$ , and the radius of the coil,  $r_0$ . It is important to note that, even when decreasing the height and increasing the coil radius lead to similar changes in the studied parameters, experimentally, increasing the radius will lead to an increase in  $Q_0$ , which is not accounted for here. Figure 8 shows the variation of resonant frequency and quality factor with  $\sigma$  as the ratio takes the values 0.2, 0.5, 1, and 2. All other parameters are the same as in Figure 5. As expected, moving the sample closer results in larger changes in both monitored parameters. In the case of resonant frequency, for very high  $\sigma$ , this can be seen as an increase in the coupling coefficient between the real coil and the imaginary mirrored coil. For the quality factor,

the transition region shifts to lower  $\sigma$  the further away from the sample we move. This is because the depth of penetration is not significantly influenced by the proximity, but the current densities are. If the coil is placed further away, the transition will occur at a larger depth of penetration (hence, lower  $\sigma$ ), as the current densities to be counterbalanced are not as large. This figure is significant from an extraction perspective as it shows that proximity is favorable for large changes which can then be easier to monitor. However, it is important to note that moving closer to a sample is experimentally challenging as stray unpredictable capacitances can be generated.

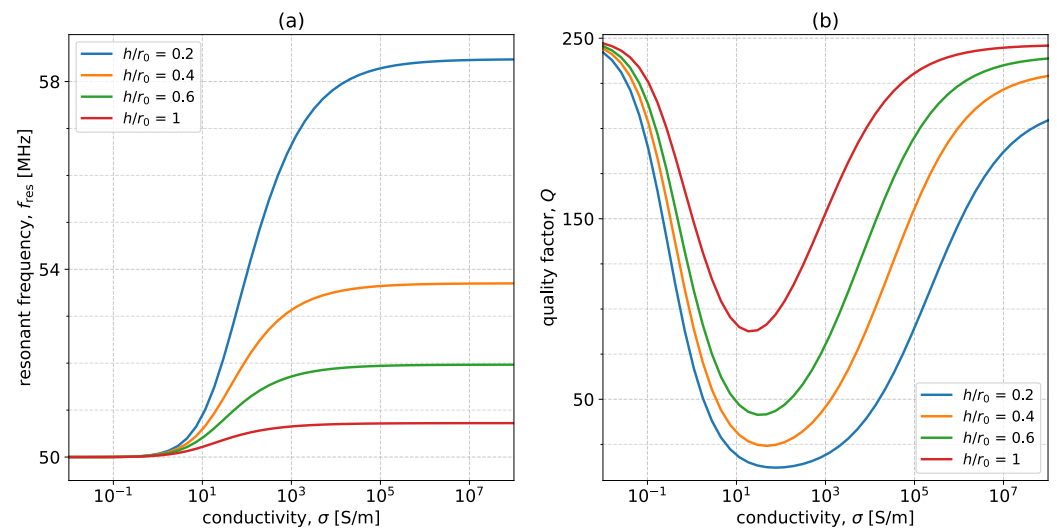


**Figure 8.** Variation of (a)  $f_{\text{res}}$  and (b)  $Q$  with  $\sigma$  for four values of  $h/r_0$ : 0.2 (blue), 0.4 (orange), 0.6 (green), and 1 (red). The other system parameters are  $w = 1$  mm,  $f_0 = 50$  MHz,  $Q_0 = 250$ ,  $t = 10$  cm, and  $\mu_r = \epsilon_r = 1$ .

The last parameter to be discussed is the free-space resonant frequency of the split-ring resonator. Figure 9 shows the variation of the normalized resonant frequency and quality factor with  $\sigma$  for 10, 20, 50, and 100 MHz. All other parameters are the same as in Figure 5. From the resonant frequency perspective, increasing the resonant frequency shifts the curves to the left, meaning that changes occur for lower conductivities. Going back to the two-coil system analogy, this is intuitive, as the sample is easier to approximate as an ideal conductor when the frequency is larger because the skin depth decreases with frequency. The same shift to the left is applicable to the quality factor plot, with the same underlying explanation: the depth of penetration decreases more quickly, hence the transitions between the two competing phenomena occur at lower conductivities. From an extraction perspective, changing the resonant frequency can be one way to target different  $\sigma$  ranges, as it offers a method of transposing the plots without interfering with the magnitude of the changes.

### 3.2. Simulated Extraction Results

Figure 10 shows the extraction error for the entire  $\sigma$  range when an artificial error of 0.01% is present in estimating  $f_{\text{res}}$  and 0.5% in estimating  $Q$ . These values are in line with the variance noticed when the parameters are measured experimentally, multiple times for the same sample. The parameters of the system are  $r_0 = 25$  mm,  $w = 1$  mm,  $h = 5$  mm,  $t = 10$  cm,  $f_0 = 50$  MHz,  $Q_0 = 250$ . The extraction was performed using  $f_{\text{res}}$  and  $Q$ , which are represented using the transparent black and red lines, respectively. The minimum error between the two extractions is then chosen. There are two breakpoints that represent the transition between the two types of extraction. In the real system, these two breakpoint frequencies will be stored for the specific geometry. If the experimental frequency is below the first breakpoint or above the second breakpoint,  $Q$  will be used for extraction; otherwise,  $f_{\text{res}}$  extraction will be performed.

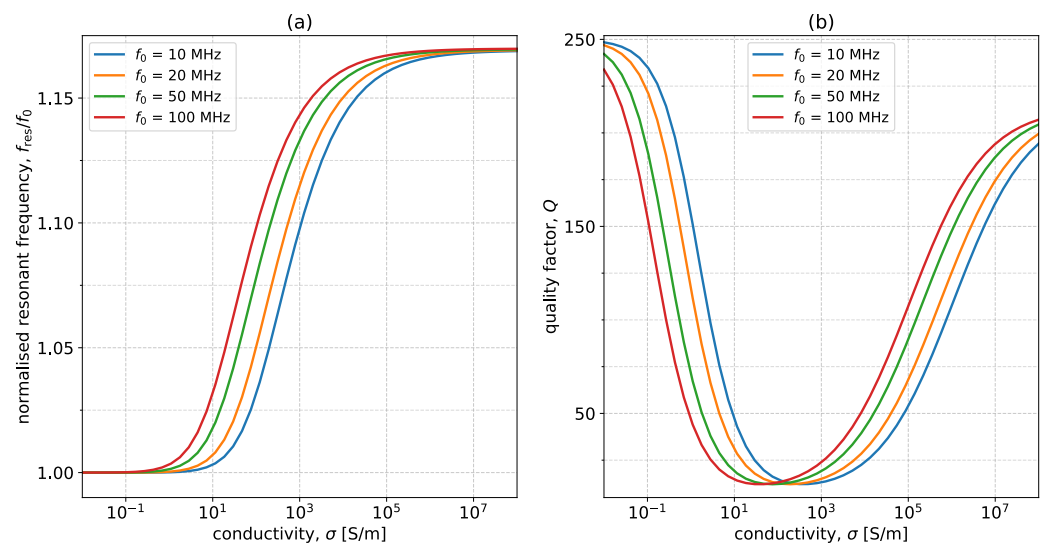


**Figure 9.** Variation of (a) normalized resonant frequency,  $f_{res}/f_0$ , and (b)  $Q$  with  $\sigma$  for four values of free-space resonant frequency,  $f_0$ : 10 MHz (blue), 20 MHz (orange), 50 MHz (green), and 100 MHz (red). The other system parameters are  $r_0 = 25$  mm,  $w = 1$  mm,  $h = 5$  mm,  $Q_0 = 250$ ,  $t = 10$  mm, and  $\mu_r = \epsilon_r = 1$ .

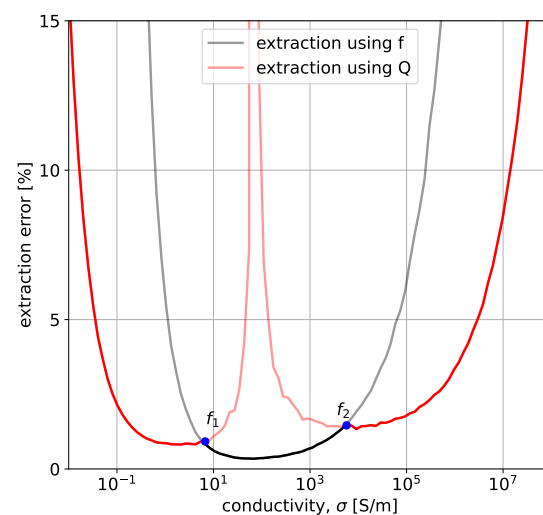


**Figure 10.** Extraction in the two presented regimes:  $f_{res}$  (black line) and  $Q$  (red line). The opaque lines represent areas where each method was chosen.  $f_1$  and  $f_2$  are cut-off frequencies for changing the selection criteria. The system parameters are  $r_0 = 25$  mm,  $w = 1$  mm,  $f_0 = 50$  MHz,  $h = 5$  mm,  $Q_0 = 250$ ,  $t = 10$  cm, and  $\mu_r = \epsilon_r = 1$ . The artificial errors are 0.01% in  $f_{res}$  and 0.5% in  $Q$ .

Figure 11 shows the extraction for different values of free-space resonant frequency,  $f_0$  (Figure 11a), and for different values of the distance to the radius ratio (Figure 11b). Starting with Figure 11a, it is noticeable that lower free-space resonant frequencies,  $f_0$ , result in better detection of large conductivities. The blue curve, corresponding to  $f_0 = 10$  MHz, is capable of detecting  $\sigma$  up to  $10^8$  S/m with an error lower than 10%. However, when looking at the low  $\sigma$  range,  $f_0 = 10$  MHz results in significant errors for conductivities below 0.1 S/m, while higher frequencies (namely 20 MHz—orange and 50 MHz—green) can detect (with an accuracy above 95%) conductivities down to 0.1 S/m. This is in line with the conclusions from Section 3.1. The same is true for Figure 11b, which shows the detection error for different height-to-radius ratios. As the probe is placed closer to the conductive material, the error decreases, and the detection range increases, especially toward the higher  $\sigma$  range. This is supported by Section 3.1, where it was shown that

decreasing the distance between the probe and the sample results in larger changes, making them easier to monitor. In conclusion, Figure 11 displays two important characteristics of the probe under study. The first one is the shift in the  $\sigma$  detection range toward high conductivities as the frequency is decreased, and the second one is the improved detection that results from minimizing the distance between the sample and the coil.

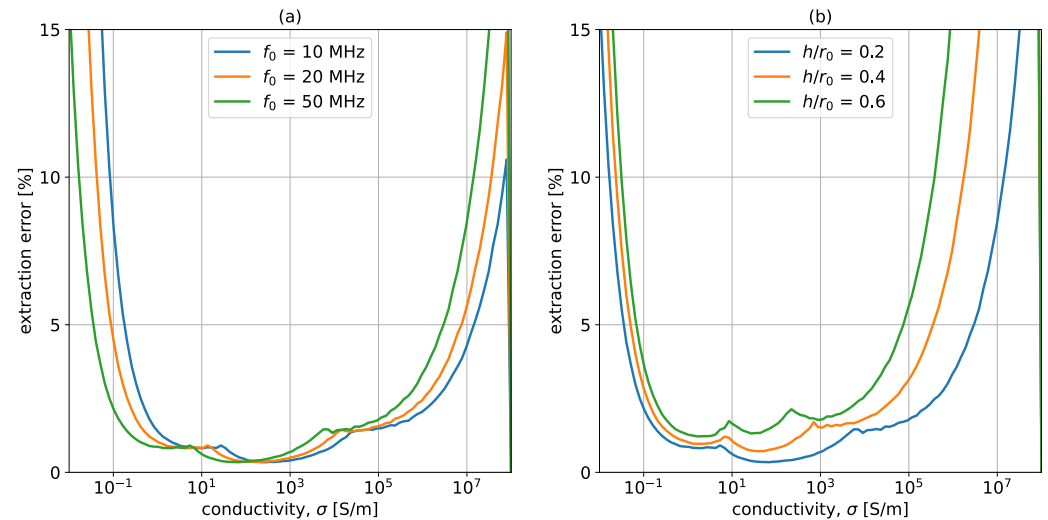


**Figure 11.** Errors in extraction for different (a) free-space frequencies,  $f_0$ , (b) height and coil radius ratios  $h/r_0$ . The artificial errors are 0.01% in  $f_{\text{res}}$  and 0.5% in  $Q$ . Unless otherwise specified in the legend, the system parameters are  $r_0 = 25$  mm,  $w = 1$  mm,  $f_0 = 50$  MHz,  $h = 5$  mm,  $Q_0 = 250$ ,  $t = 10$  cm, and  $\mu_r = \epsilon_r = 1$ .

### 3.3. Experimental Results for Low Conductivity Samples

#### 3.3.1. Comparison of $f$ and $Q$

Figure 12 shows the variation of  $f_{\text{res}}$  and  $Q$  as conductivity is increased up to 20 S/m in the system described in Section 2.3. The data are presented for the analytical model (blue solid line), the raw experimental data (red data points), the smoothed experimental data (blue data points), and CST Microwave Studio data (black dashed line). The experimental data points are presented using error bars for which the mean and the variance were obtained from the 20 experimental points taken for each  $\sigma$ . From the figure, it can be seen that the variance is significantly decreased once the data are smoothed. It is important to note that the data were normalized to the first point corresponding to water without salt ( $\sigma = 0.04$  S/m). This normalization is necessary because the water layer interacts with the metallic plate of the SMA connector, which increases the capacitance of the coil. The same normalization was performed for the CST data to ensure that the first point in the  $\sigma$  sweep corresponds to the first point in the experimental data. It can be seen that the match is very good, indicating that conductivity detection is possible.

#### 3.3.2. Extraction Results

Figure 13 shows the results of extracting conductivity from the experimental data using the analytical model (red line) and the CST data (blue dots). The red transparent filled-in curve represents the entire range of conductivities extracted when one takes into account the 0.11 mm height uncertainty. The extraction from CST data was conducted by interpolating between the pre-stored CST values. All the extractions were performed using  $Q$  as the main extraction parameter. The analytical model performs better in extraction compared to the CST one. Conductivities of up to 12.5 S/m are detected with an error lower than 10% while conductivities of up to 5.5 S/m are detected with an error of below 5%. Most importantly, using the quality factor as a separation criterion proves to be an effective technique for distinguishing between very low  $\sigma$  samples. As shown in Table 2, the mean error in detection for conductivities lower than 1 S/m is 4.5%.

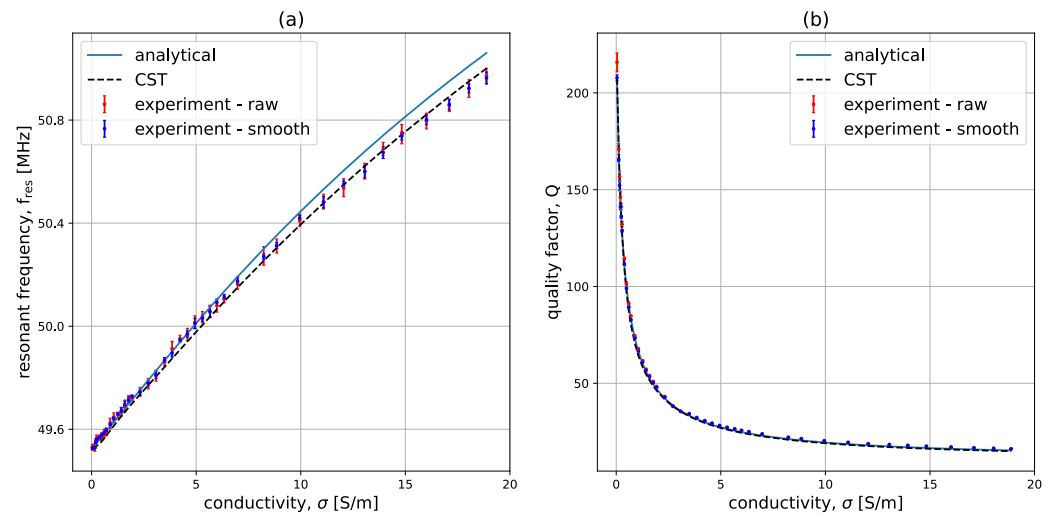


**Figure 12.** Variation of (a)  $f_{res}$ , and (b)  $Q$  with  $\sigma$  in the analytical model (blue solid line), the raw experimental data (red data points), the smoothed experimental data (blue data points), CST Microwave Studio data (black dashed line). The system parameters are  $r_0 = 25$  mm,  $w = 1.04$  mm,  $h = 5.32 \pm 0.11$  mm,  $f_0 = 49.777$  MHz,  $Q_0 = 256$ ,  $t = 10$  cm,  $\mu_r = 1$ , and  $\epsilon_r = 80$ .

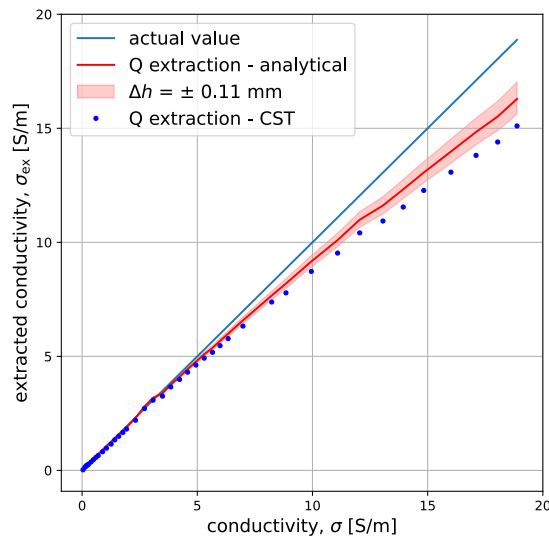


**Figure 13.** Extracted conductivity from the analytical model (red line) with the error bar for height uncertainty (red transparent area) and from CST data (blue dots). The parameters of the system are  $r_0 = 25$  mm,  $w = 1.04$  mm,  $h = 5.32 \pm 0.11$  mm,  $f_0 = 49.777$  MHz,  $Q_0 = 256$ ,  $t = 10$  cm,  $\mu_r = 1$ , and  $\epsilon_r = 80$ .

**Table 2.** Comparison between the mean error in conductivity extraction using the analytical model and the CST numerical results for different conductivity ranges.

Range	Nb. of Samples	Analytical Extraction	CST Extraction
$\sigma < 1$ S/m	11	4.5%	9.2%
$\sigma < 5$ S/m	25	3.0%	7.1%
$\sigma < 12.5$ S/m	35	3.9%	7.9%
$\sigma < 20$ S/m	42	5.5%	9.7%

Table 2 compares the mean performance of the analytical extraction with the interpolation extraction using CST for different ranges of conductivity. For each range of

conductivity, the number of samples considered is shown in the second column. While the analytical model has a mean error lower than 5.5% for the entire range considered, the error using the numerical solver is higher (almost 10%).

The extraction error is also influenced by the accuracy with which we can estimate the height,  $h$ . When the height,  $h$ , is deviated by 0.11 mm (approximated to be the error in estimating the distance for the presented experiment), the mean extraction error for the analytical model goes from 5.5% to 6.6%. This suggests that accurate height measurements should be prioritized when implementing the method.

#### 4. Discussion and Conclusions

A method for remotely detecting conductivity using the quality factor and the resonant frequency of a single split-ring resonator is presented. The analytical model used for this method is outlined and the choice of coil parameters is discussed using analytical parametric plots. In order to optimize detection, it is suggested that the coil radius be as large as possible and the distance from the sample is as small as possible. The free space resonant frequency of the coil should be low (in the range of 1–10 MHz) for high conductivity samples and larger (in the range of 50–100 MHz) for medium and low conductivity ones. Experimental data are presented for a sample with low conductivity and detection with an error below 10% is achieved for conductivities below 12.5 S/m. It is concluded that detection in the full range is possible and that detecting conductivities down to 0.1 S/m is achievable. More importantly, it is proven that using this method and the chosen optimization parameters, one can distinguish between samples with very low conductivities, such as human tissue. Separating different types of body tissue conductivities is highly relevant as it enables research into abnormalities detection (such as water in the lungs) and holds significant importance for body imaging, particularly in induction tomography. Considering that very little power is used for sensing (1 mW), the specific absorption rates inside human tissues are lower than 0.1 W/kg. This is significantly below the safety limit of 2 W/kg, making further development of such a method for body imaging attractive from a safety perspective.

**Author Contributions:** Conceptualization, G.D., A.R., C.J.S., L.S. and E.S.; Data curation, G.D., A.R., C.J.S., L.S. and E.S.; Formal analysis, G.D., A.R., C.J.S., L.S. and E.S.; Funding acquisition, C.J.S. and E.S.; Investigation, G.D., A.R., C.J.S. and E.S.; Methodology, G.D., A.R., C.J.S. and E.S.; Project administration, A.R., C.J.S. and E.S.; Resources, G.D., A.R., C.J.S., L.S. and E.S.; Software, G.D. and E.S.; Supervision, A.R., C.J.S. and E.S.; Validation, G.D., A.R. and E.S.; Visualization, G.D. and E.S.; Writing—original draft, G.D.; Writing—review & editing, G.D., A.R., C.J.S., L.S. and E.S. All authors have read and agreed to the published version of the manuscript.

**Funding:** We gratefully acknowledge the financial support from the EPSRC UK (SYMETA grant EP/N010493/1) and by an anonymous donor in the USA.

**Institutional Review Board Statement:** Not applicable.

**Informed Consent Statement:** Not applicable.

**Data Availability Statement:** Data are contained within the article.

**Acknowledgments:** We extend our gratitude to our colleagues from the OxiMeta network and the Oxford Communications Engineering group for the engaging and productive discussions.

**Conflicts of Interest:** The authors declare no conflict of interest. The funders had no role in the design of the study; in the collection, analyses, or interpretation of data; in the writing of the manuscript; or in the decision to publish the results.

#### Appendix A. Vector Potential in a Stratified Geometry

The derivation of the vector potential  $\mathbf{A}$  in each of the four regions of Figure 1 starts from:

$$\nabla^2 \mathbf{A} = -\mu \mathbf{i}_0 + \mu \sigma \frac{\partial \mathbf{A}}{\partial t} + \mu \epsilon \frac{\partial^2 \mathbf{A}}{\partial t^2} + \mu \nabla \left( \frac{1}{\mu} \right) \times (\nabla \times \mathbf{A}) \quad (\text{A1})$$

where  $\mathbf{i}_0$  is the current density,  $\mu$  is the permeability,  $\sigma$  denotes conductivity, and  $\varepsilon$  denotes permittivity.

Assuming axial symmetry, there is only an azimuthal component,  $\theta$ , of the vector potential:  $\mathbf{A} = A\mathbf{i}_\theta$  and  $\mathbf{i}_0 = i_0\mathbf{i}_\theta$ ; the equation becomes

$$\frac{\partial^2 A}{\partial r^2} + \frac{1}{r} \frac{\partial A}{\partial r} + \frac{\partial^2 A}{\partial z^2} - \frac{A}{r^2} = -\mu i_0 + \mu\sigma \frac{\partial A}{\partial t} + \mu\varepsilon \frac{\partial^2 A}{\partial t^2} - \mu \frac{1}{r} \frac{\partial(1/\mu)}{\partial r} \frac{\partial(rA)}{\partial r} - \mu \frac{\partial(1/\mu)}{\partial z} \frac{\partial A}{\partial z} \quad (\text{A2})$$

If  $A$  and  $i_0$  are harmonic functions of time [ $A = A' \exp(j\omega t)$  and  $i_0 = i'_0 \exp(j\omega t)$ ], and if the media are homogeneous (hence,  $\mu$  and  $\varepsilon$  are independent on  $r$  and  $z$ ), then the above equation simplifies to

$$\frac{\partial^2 A'}{\partial r^2} + \frac{1}{r} \frac{\partial A'}{\partial r} + \frac{\partial^2 A'}{\partial z^2} - \frac{A'}{r^2} = -\mu i'_0 + j\omega\mu\sigma A' - \omega^2\mu\varepsilon A' \quad (\text{A3})$$

Assuming that the coil is filamentary, then

$$I = \frac{i'_0}{\delta(r-r_0)\delta(z-z_0)} \quad (\text{A4})$$

$$\frac{\partial^2 A'}{\partial r^2} + \frac{1}{r} \frac{\partial A'}{\partial r} + \frac{\partial^2 A'}{\partial z^2} - \frac{A'}{r^2} = -\mu I \delta(r-r_0)\delta(z-z_0) + j\omega\mu\sigma A' - \omega^2\mu\varepsilon A' \quad (\text{A5})$$

Inside the four layers, there is no excitation, hence

$$\frac{\partial^2 A'}{\partial r^2} + \frac{1}{r} \frac{\partial A'}{\partial r} + \frac{\partial^2 A'}{\partial z^2} - \frac{A'}{r^2} - j\omega\mu\sigma A' + \omega^2\mu\varepsilon A' = 0 \quad (\text{A6})$$

Using the separation of variables,  $A'(r, z) = R(r)Z(z)$ , we obtain two new differential equations (Equations (A8) and (A9)):

$$\frac{1}{R(r)} \frac{d^2 R(r)}{dr^2} + \frac{1}{rR(r)} \frac{dR(r)}{dr} + \frac{1}{Z(z)} \frac{d^2 Z(z)}{dz^2} - \frac{1}{r^2} - j\omega\mu\sigma + \omega^2\varepsilon\mu = 0 \quad (\text{A7})$$

$$\frac{1}{R(r)} \frac{d^2 R(r)}{dr^2} + \frac{1}{rR(r)} \frac{dR(r)}{dr} - \frac{1}{r^2} + \alpha^2 = 0 \quad (\text{A8})$$

$$\frac{1}{Z(z)} \frac{d^2 Z(z)}{dz^2} = \alpha^2 + j\omega\mu\sigma - \omega^2\varepsilon\mu \quad (\text{A9})$$

Defining  $\alpha_n = \sqrt{\alpha^2 + j\omega\mu\sigma - \omega^2\varepsilon\mu}$ , where  $n$  is the index of the layer for which the equation is solved and solving Equation (A9) leads to

$$Z(z) = B_n(\alpha)e^{z\alpha_n} + C_n(\alpha)e^{-z\alpha_n} \quad (\text{A10})$$

where  $B_n$  and  $C_n$  are coefficients corresponding to region  $n$ .

Equation (A8) is a first-order Bessel equation; hence, the non-diverging solution in the  $n^{\text{th}}$  layer can be written as

$$R(r) = D_n(\alpha)J_1(\alpha r) \quad (\text{A11})$$

where  $J_1$  is the Bessel function of the first-order and first kind.

Therefore, the vector potential in each region is

$$A_n(r, z) = \int_0^\infty [B_n(\alpha)e^{z\alpha_n} + C_n(\alpha)e^{-z\alpha_n}] D_n(\alpha) J_1(\alpha r) d\alpha \equiv \int_0^\infty [X_n(\alpha)e^{z\alpha_n} + W_n(\alpha)e^{-z\alpha_n}] J_1(\alpha r) d\alpha \quad (\text{A12})$$

To prevent divergence in regions  $I$  and  $IV$ , where  $z \rightarrow \infty$  in region  $I$  and  $z \rightarrow -\infty$  in region  $IV$ , we set  $X_I = 0$  and  $W_{IV} = 0$ . The other coefficients are found by imposing boundary conditions. The general boundary conditions between layer  $n$  and layer  $n + 1$  for

any system are  $B_{\perp n} = B_{\perp n+1}$  and  $H_{\parallel n} = H_{\parallel n+1}$ . As  $\mathbf{B}_n = \Delta \times \mathbf{A} = -\frac{\partial A_n}{\partial z} \mathbf{i}_r + \frac{1}{r} \frac{\partial(rA_n)}{\partial r} \mathbf{i}_z$ , where the  $z$  direction is the normal component and the radial direction is the tangential one, the two boundary conditions are

$$\left( \frac{1}{r} A_n + r \frac{\partial A_n}{\partial r} \right) \Big|_{z=z_n} = \left( \frac{1}{r} A_{n+1} + r \frac{\partial A_{n+1}}{\partial r} \right) \Big|_{z=z_n} \implies A_n = A_{n+1} \quad (\text{A13})$$

$$\left( \frac{1}{\mu_n} \frac{\partial A_n}{\partial z} \right) \Big|_{z=z_n} = \left( \frac{1}{\mu_{n+1}} \frac{\partial A_{n+1}}{\partial z} \right) \Big|_{z=z_n} \quad (\text{A14})$$

The following equations are the boundary conditions for the structure with four layers:

$$W_I e^{-h\alpha_I} = X_{II} e^{h\alpha_{II}} + W_{II} e^{-h\alpha_{II}} \quad (\text{A15})$$

$$-\alpha_I W_I e^{-h\alpha_I} = \alpha_{II} X_{II} e^{h\alpha_{II}} - \alpha_{II} W_{II} e^{-h\alpha_{II}} - \gamma \quad (\text{A16})$$

$$X_{II} + W_{II} = X_{III} + W_{III} \quad (\text{A17})$$

$$\alpha_{II} X_{II} - \alpha_{II} W_{II} = \alpha_{III} X_{III} - \alpha_{III} W_{III} \quad (\text{A18})$$

$$X_{III} e^{-t\alpha_{III}} + W_{III} e^{t\alpha_{III}} = X_{IV} e^{-t\alpha_{IV}} \quad (\text{A19})$$

$$\alpha_{III} X_{III} e^{-t\alpha_{III}} - \alpha_{III} W_{III} e^{t\alpha_{III}} = \alpha_{IV} X_{IV} e^{-t\alpha_{IV}} \quad (\text{A20})$$

where  $\gamma = \mu_0 I r_0 J_1(\alpha r_0) \alpha_I = \alpha_{II} = \alpha_{IV}$  since all these layers are assumed to be air. To simplify the following equations,  $\alpha_I = \alpha_{II} = \alpha_{IV} \equiv \alpha_0$  and  $\alpha_{III} = \alpha_1$ . Solving this system of equations leads to coefficients corresponding to each layer:

$$X_{II} = \frac{1}{2} \mu_0 I J_1(\alpha r_0) r_0 e^{-\alpha_0 h} \quad (\text{A21})$$

$$X_{III} = \mu_0 I J_1(\alpha r_0) r_0 \frac{\alpha_0(\alpha_0 + \alpha_1) e^{-\alpha_0 h} e^{2\alpha_1 t}}{(\alpha_1 + \alpha_0)^2 e^{2\alpha_1 t} - (\alpha_0 - \alpha_1)^2} \quad (\text{A22})$$

$$X_{IV} = \mu_0 I J_1(\alpha r_0) r_0 \frac{2\alpha_1 \alpha_0 e^{-\alpha_0 h} e^{t(\alpha_1 + \alpha_0)}}{(\alpha_1 + \alpha_0)^2 e^{2\alpha_1 t} - (\alpha_0 - \alpha_1)^2} \quad (\text{A23})$$

$$W_I = \frac{1}{2} \mu_0 I J_1(\alpha r_0) r_0 \left( e^{\alpha_0 h} + \frac{1}{2} e^{-\alpha_0 h} \frac{(\alpha_0^2 - \alpha_1^2) - (\alpha_1^2 - \alpha_0^2) e^{2\alpha_1 t}}{(\alpha_1 + \alpha_0)^2 e^{2\alpha_1 t} - (\alpha_0 - \alpha_1)^2} \right) \quad (\text{A24})$$

$$W_{II} = \frac{1}{2} \mu_0 I J_1(\alpha r_0) r_0 \frac{(\alpha_0^2 - \alpha_1^2) e^{-\alpha_0 h} (e^{2\alpha_1 t} - 1)}{(\alpha_1 + \alpha_0)^2 e^{2\alpha_1 t} - (\alpha_0 - \alpha_1)^2} \quad (\text{A25})$$

$$W_{III} = \mu_0 I J_1(\alpha r_0) r_0 \frac{\alpha_0(\alpha_0 - \alpha_1) e^{-\alpha_0 h}}{(\alpha_1 + \alpha_0)^2 e^{2\alpha_1 t} - (\alpha_0 - \alpha_1)^2} \quad (\text{A26})$$

Having found the vector potential in each region, as

$$A_n(r, z) = \int_0^\infty [X_n(\alpha) e^{z\alpha_n} + W_n(\alpha) e^{-z\alpha_n}] J_1(\alpha r) d\alpha \quad (\text{A27})$$

it is possible to calculate the mutual inductance between two filament coils, as

$$M = \frac{1}{I} \oint_L \mathbf{A} \cdot d\mathbf{l} = \frac{1}{I} \int_0^{2\pi} A_n(\phi) \rho(\phi) d\phi \quad (\text{A28})$$

where  $\rho$  is the distance between the center of the excited coil and the track of the receiving coil. When calculating the self-inductance of a coil, we consider the pseudo-receiving coil to be  $R_{\text{GMD}}$  underneath the transmitting coil.

$$\log R_{\text{GMD}} = \log \frac{w}{2} - \frac{w_1^4}{(w^2 - w_1^2)^2} \log \frac{w}{w_1} + \frac{3w_1^2 - w^2}{4(w^2 - w_1^2)} \quad (\text{A29})$$

where  $w$  is the outer area of the section where the current flows in the wire and  $w_i$  is the inner area of the section where the current flows in the wire ( $w_i = w - \delta$ , where  $\delta = \sqrt{\frac{2}{\sigma\mu\omega}}$  is the skin depth of the wire material).

The inductance, therefore, uses the vector potential from region II. Assuming the two coils are spaced  $R_{\text{GMD}}/2$  and  $-R_{\text{GMD}}/2$ , with respect to the center of the coil, which is at height  $h$ , the inductance is

$$L = \pi r_0^2 \mu_0 \int_0^\infty \alpha_0 J_1^2(\alpha r_0) \left( e^{\alpha_0 R_{\text{GMD}}} + \frac{(\alpha_0^2 - \alpha_1^2) e^{-\alpha_0 2h} (e^{2\alpha_1 t} - 1)}{(\alpha_1 + \alpha_0)^2 e^{2\alpha_1 t} - (\alpha_0 - \alpha_1)^2} \right) d\alpha \quad (\text{A30})$$

## References

- García-Martín, J.; Gómez-Gil, J.; Vázquez-Sánchez, E. Non-destructive techniques based on eddy current testing. *Sensors* **2011**, *11*, 2525–2565. [[CrossRef](#)]
- Sophian, A.; Tian, G.; Taylor, D.; Rudlin, J. Electromagnetic and eddy current NDT: A review. *Insight* **2001**, *43*, 302–306.
- Khajeh-Khalili F.; Honarvar, M.A. Novel Tunable Peace-Logo Planar Metamaterial Unit-Cell for Millimeter-Wave Applications. *ETRI J.* **2018**, *40*, 389–395. [[CrossRef](#)]
- Rifai, D.; Abdalla, A.N.; Ali, K.; Razali, R. Giant magnetoresistance sensors: A review on structures and non-destructive eddy current testing applications. *Sensors* **2016**, *16*, 298. [[CrossRef](#)] [[PubMed](#)]
- Gong, Z.; Yang, S. Metamaterial-core probes for nondestructive eddy current testing. *IEEE Trans. Instrum. Meas.* **2020**, *70*, 1–9. [[CrossRef](#)]
- Savin, A.; Bruma, A.; Steigmann, R.; Iftimie, N.; Faktorova, D. Enhancement of spatial resolution using a metamaterial sensor in nondestructive evaluation. *Appl. Sci.* **2015**, *5*, 1412–1430. [[CrossRef](#)]
- Meng, X.; Lu, M.; Yin, W.; Bennecer, A.; Kirk, K.J. Evaluation of coating thickness using lift-off insensitivity of eddy current sensor. *Sensors* **2021**, *21*, 419. [[CrossRef](#)] [[PubMed](#)]
- Yin, W.; Peyton, A. Thickness measurement of non-magnetic plates using multi-frequency eddy current sensors. *NDT E Int.* **2007**, *40*, 43–48. [[CrossRef](#)]
- Shin, Y.-K.; Choi, D.-M.; Kim, Y.-J.; Lee, S.-S. Signal characteristics of differential-pulsed eddy current sensors in the evaluation of plate thickness. *NDT E Int.* **2009**, *42*, 215–221. [[CrossRef](#)]
- Moulder, J.C.; Uzal, E.; Rose, J.H. Thickness and conductivity of metallic layers from eddy current measurements. *Rev. Sci. Instrum.* **1992**, *63*, 3455–3465. [[CrossRef](#)]
- Pan, Y.-L.; Tai, C.-C. Thickness and conductivity analysis of molybdenum thin film in CIGS solar cells using resonant electromagnetic testing method. *IEEE Trans. Magn.* **2012**, *48*, 347–350. [[CrossRef](#)]
- Tai, C.-C.; Rose, J.H.; Moulder, J.C. Thickness and conductivity of metallic layers from pulsed eddy-current measurements. *Rev. Sci. Instrum.* **1996**, *67*, 3965–3972. [[CrossRef](#)]
- Xu, J.; Wu, J.; Xin, W.; Ge, Z. Fast measurement of the coating thickness and conductivity using eddy currents and plane wave approximation. *IEEE Sens. J.* **2020**, *21*, 306–314. [[CrossRef](#)]
- Burkhardt, J. Determination of the conductivity and thickness of conductive layers on conductive base materials. *Adv. Mech. Eng.* **2019**, *11*, 1687814019854234. [[CrossRef](#)]
- Said, N.; Abu-Nabah, B.A.; Alkhader, M. Triple-frequency eddy current estimation of nonmagnetic metal clad thicknesses over nonmagnetic metals. *Measurement* **2021**, *182*, 109668. [[CrossRef](#)]
- Xue, Z.; Fan, M.; Cao, B.; Wen, S. Enhancement of thickness measurement in eddy current testing using a log-log method. *J. Nondestruct. Eval.* **2021**, *40*, 1–10. [[CrossRef](#)]
- Le, C.D. Eddy Current Measurements of Thin-Film Metal Coatings Using a Selectable Calibration Standard. U.S. Patent 6,549,006, 15 April 2003.
- Ali, K.B.; Abdalla, A.N.; Rifai, D.; Faraj, M.A. Review on system development in eddy current testing and technique for defect classification and characterization. *IET Circuits Devices Syst.* **2017**, *11*, 338–351. [[CrossRef](#)]
- Cheng, L.; Tian, G.Y. Surface crack detection for carbon fiber reinforced plastic (CFRP) materials using pulsed eddy current thermography. *IEEE Sens. J.* **2011**, *11*, 3261–3268. [[CrossRef](#)]
- Zenzinger, G.; Bamberg, J.; Satzger, W.; Carl, V. Thermographic crack detection by eddy current excitation. *Nondestruct. Test. Eval.* **2007**, *22*, 101–111. [[CrossRef](#)]
- Chady, T.; Enokizono, M.; Sikora, R. Crack detection and recognition using an eddy current differential probe. *IEEE Trans. Magn.* **1999**, *35*, 1849–1852. [[CrossRef](#)]
- Tian, G.Y.; Sophian, A.; Taylor, D.; Rudlin, J. Multiple sensors on pulsed eddy-current detection for 3D subsurface crack assessment. *IEEE Sens. J.* **2005**, *5*, 90–96. [[CrossRef](#)]
- Nakagawa, N. A model of eddy current nondestructive evaluation for a current leaking crack. *NDT E Int.* **2021**, *123*, 102517. [[CrossRef](#)]

24. Sun, H.; Yi, J.; Wang, T.; Wang, Y.; Qing, X. A new interleaving eddy current array-based sensing film for fatigue crack quantification of bolted joints. *J. Intell. Mater. Syst. Struct.* **2021**, *32*, 1867–1877. [[CrossRef](#)]
25. Yu, Y.; Gao, K.; Theodoulidis, T.; Yuan, F. Analytical solution for magnetic field of cylindrical defect in eddy current nondestructive testing. *Phys. Scr.* **2019**, *95*, 015501. [[CrossRef](#)]
26. Cung, L.T.; Dao, T.D.; Nguyen, P.C.; Bui, T.D. A model-based approach for estimation of the crack depth on a massive metal structure. *Meas. Control* **2018**, *51*, 182–191. [[CrossRef](#)]
27. Kuyvenhoven, N.; Dean, C.; Melton, J.; Schwannecke, J.; Umenei, A. Development of a foreign object detection and analysis method for wireless power systems. In Proceedings of the 2011 IEEE Symposium on Product Compliance Engineering, San Diego, CA, USA, 10–12 October 2011; pp. 1–6.
28. Chana, K.; Cardwell, D. The use of eddy current sensor based blade tip timing for FOD detection. In Proceedings of the Turbo Expo: Power for Land, Sea, and Air, Berlin, Germany, 9–13 June 2008; pp. 169–178.
29. Loete, F.; Le Bihan, Y.; Mencaraglia, D. Contactless device for the fast conductivity characterization of a large range semiconductors. In Proceedings of the 2016 International Symposium on Semiconductor Manufacturing (ISSM), Tokyo, Japan, 12–13 December 2016; pp. 1–4.
30. Bowler, N.; Huang, Y. Electrical conductivity measurement of metal plates using broadband eddy current and four-point methods. *Meas. Sci. Technol.* **2005**, *16*, 2193. [[CrossRef](#)]
31. Yin, W.; Peyton, A.J.; Zysko, G.; Denno R. Simultaneous noncontact measurement of water level and conductivity. *IEEE Trans. Instrum. Meas.* **2008**, *57*, 2665–2669.
32. Wang, C.; Fan, M.; Cao, B.; Ye, B.; Li, W. Novel noncontact eddy current measurement of electrical conductivity. *IEEE Sens. J.* **2018**, *18*, 9352–9359. [[CrossRef](#)]
33. Lu M.; Meng, X.; Huang, R.; Chen, L.; Peyton, A.; Yin, W. A high-frequency phase feature for the measurement of magnetic permeability using eddy current sensor. *NDT E Int.* **2021**, *123*, 102519. [[CrossRef](#)]
34. Lu M.; Meng, X.; Chen, L.; Huang, R.; Yin, W.; Peyton, A. Measurement of ferromagnetic slabs permeability based on a novel planar triple-coil sensor. *IEEE Sens. J.* **2019**, *20*, 2904–2910. [[CrossRef](#)]
35. Desjardins, D.; Krause, T.; Clapham, L. Transient eddy current method for the characterization of magnetic permeability and conductivity. *NDT E Int.* **2016**, *80*, 65–70. [[CrossRef](#)]
36. Flowers, P.F.; Reyes, C.; Ye, S.; Kim, M.J.; Wiley, B.J. 3D printing electronic components and circuits with conductive thermoplastic filament. *Addit. Manuf.* **2017**, *18*, 156–163. [[CrossRef](#)]
37. Khan, A.; Rahman, K.; Kim, D.S.; Choi, K.H. Direct printing of copper conductive micro-tracks by multi-nozzle electrohydrodynamic inkjet printing process. *J. Mater. Process. Technol.* **2012**, *212*, 700–706. [[CrossRef](#)]
38. Hong, C.M.; Wagner, S. Inkjet printed copper source/drain metallization for amorphous silicon thin-film transistors. *IEEE Electron. Device Lett.* **2000**, *21*, 384–386. [[CrossRef](#)]
39. Park, J.-U.; Lee, S.; Unarunotai, S.; Sun, Y.; Dunham, S.; Song, T.; Ferreira, P.M.; Alleyene, A.G.; Paik, U.; Rogers, J.A. Nanoscale, electrified liquid jets for high-resolution printing of charge. *Nano Lett.* **2010**, *10*, 584–591. [[CrossRef](#)]
40. Jian, J.R.; Kim, T.; Park, J.S.; Wang, J.; Kim, W.S. High performance 3D printed electronics using electroless plated copper. *AIP Adv.* **2017**, *7*, 035314. [[CrossRef](#)]
41. Kim, M.J.; Cruz, M.A.; Ye, S.; Gray, A.L.; Smith, S.L.; Lazarus, N.; Walker, C.J.; Sigmarsson, H.H.; Wiley, B.J. One-step electrodeposition of copper on conductive 3D printed objects. *Addit. Manuf.* **2019**, *27*, 318–326. [[CrossRef](#)]
42. Tan, J.; Low, H. Embedded electrical tracks in 3D printed objects by fused filament fabrication of highly conductive composites. *Addit. Manuf.* **2018**, *23*, 294–302. [[CrossRef](#)]
43. Kwok, S.W.; Goh, K.H.H.; Tan, Z.D.; Tan, S.T.M.; Tjiu, W.W.; Soh, J.Y.; Ng, Z.J.G.; Chan, Y.Z.; Hui, H.K.; Goh, K.E.J. Electrically conductive filament for 3D-printed circuits and sensors. *Appl. Mater. Today* **2017**, *9*, 167–175. [[CrossRef](#)]
44. Xie, Y.; Ye, S.; Reyes, C.; Sithikong, P.; Popa, B.-I.; Wiley, B.J.; Cummer, S.A. Microwave metamaterials made by fused deposition 3D printing of a highly conductive copper based filament. *Appl. Phys. Lett.* **2017**, *110*, 181903. [[CrossRef](#)]
45. Zhang, D.; Chi, B.; Li, B.; Gao, Z.; Du, Y.; Guo, J.; Wei, J. Fabrication of highly conductive graphene flexible circuits by 3D printing. *Synth. Met.* **2016**, *217*, 79–86. [[CrossRef](#)]
46. Sekine, T.; Ito, K.; Shouji, Y.; Suga, R.; Yasuda, T.; Wang, Y.-F.; Takeda, Y.; Kumaki, D.; Santos, F.D.D.; Tong, H.; et al. Robotic e-skin for high performance stretchable acceleration sensor via combinations of novel soft and functional polymers. *Appl. Mater. Today* **2023**, *33*, 101877. [[CrossRef](#)]
47. Mansor, M.S.; Zakaria, Z.; Balkhis, I.; Sahib, M.; Yunos, Y.; Sahlan, S.; Bunyamin, S.; Abas, K.H.; Ishak, M.; Danapalasingam, K.A. Magnetic induction tomography: A brief review. *J. Teknol.* **2015**, *73*, 91–95.
48. Griffiths, H. Magnetic induction tomography. *Meas. Sci. Technol.* **2001**, *12*, 1126. [[CrossRef](#)]
49. Gabriel, C.; Gabriel, S.; Corthout, Y.E. The dielectric properties of biological tissues: I. literature survey. *Phys. Med. Biol.* **1996**, *41*, 2231. [[CrossRef](#)]
50. Gabriel, S.; Lau, R.; Gabriel, C. The dielectric properties of biological tissues: III. parametric models for the dielectric spectrum of tissues. *Phys. Med. Biol.* **1996**, *41*, 2271. [[CrossRef](#)]
51. Gabriel, S.; Lau, R.; Gabriel, C. The dielectric properties of biological tissues: II. measurements in the frequency range 10 Hz to 20 GHz. *Phys. Med. Biol.* **1996**, *41*, 2251. [[CrossRef](#)] [[PubMed](#)]

52. Shahrestani, S.; Chou, T.-C.; Shang, K.-M.; Zada, G.; Borok, Z.; Rao, A.P.; Tai, Y.-C. A wearable eddy current based pulmonary function sensor for continuous non-contact point-of-care monitoring during the COVID-19 pandemic. *Sci. Rep.* **2021**, *11*, 20144. [[CrossRef](#)] [[PubMed](#)]
53. Richer, A.; Adler, A. Eddy current based flexible sensor for contactless measurement of breathing. In Proceedings of the 2005 IEEE Instrumentation and Measurement Technology Conference, Ottawa, ON, Canada, 17–19 May 2005; pp. 623–626.
54. Dodd, C.; Deeds, W. Analytical solutions to eddy-current probe-coil problems. *J. Appl. Phys.* **1968**, *39*, 2829–2838. [[CrossRef](#)]
55. Dodd, C.V. Solutions to Electromagnetic Induction Problems. Ph.D. Thesis, The University of Tennessee, Knoxville, TN, USA, 1967.
56. Vallecchi, A.; Chu, S.; Solymar, L.; Stevens, C.; Shamonina, E. Coupling between coils in the presence of conducting medium. *IET Microw. Antennas Propag.* **2018**, *13*, 55–62. [[CrossRef](#)]
57. Vallecchi, A.; Stevens, C.; Shamonina, E. Wireless power transfer in the presence of a conducting interface: An analytical solution. In Proceedings of the Loughborough Antennas Propagation Conference 2017, Loughborough, UK, 13–14 November 2017; pp. 725–731.
58. Maxwell, J.C. *Electricity and Magnetism*; Dover New York: New York, NY, USA, 1954.
59. Rosa, E.B.; Grover, F.W. *Formulas and Tables for the Calculation of Mutual and Self-Inductance*; US Government Printing Office: Washington, DC, USA, 1948.
60. Abu-Nabah, B.A. Reduction of lift-off effect in high-frequency apparent eddy current conductivity spectroscopy. *Meas. Sci. Technol.* **2017**, *28*, 055107. [[CrossRef](#)]
61. Dzikowski, L. Elimination of coil liftoff from eddy current measurements of conductivity. *IEEE Trans. Instrum. Meas.* **2013**, *62*, 555–565. [[CrossRef](#)]

**Disclaimer/Publisher’s Note:** The statements, opinions and data contained in all publications are solely those of the individual author(s) and contributor(s) and not of MDPI and/or the editor(s). MDPI and/or the editor(s) disclaim responsibility for any injury to people or property resulting from any ideas, methods, instructions or products referred to in the content.